OPEN ACCESS

Saudi Journal of Engineering and Technology

Abbreviated Key Title: Saudi J Eng Technol
ISSN 2415-6272 (Print) |ISSN 2415-6264 (Online)
Scholars Middle East Publishers, Dubai, United Arab Emirates
Journal homepage: https://saudijournals.com

Review Article

Dynamic Anion Sublattices, Cooperative Ion Migration and Metastable Pathway Engineering for Next-Generation Solid Electrolytes

Rajab Abbas[1]*, Rabia Shahzad[2], Aasma Bibi[3], Muhammad Adeel[4], Muhammad Usman[5], Rizwan Haider[5], Waqar Yousaf[6], Hunza Afzal[5], Junaid Zaman[5]

[1]Department of Materials Science and Engineering, Ghulam Ishaq Khan Institute of Engineering Sciences and Technology, Topi, Khyber Pakhtunkhwa, Pakistan
[2]State Key Laboratory of Metastable Materials Science and Technology, School of Materials Science and Engineering, Yanshan University, Qinhuangdao 066004, China
[3]Department of Chemistry, University of the Punjab, Quaid-i-Azam Campus, Lahore 54590, Punjab, Pakistan
[4]Department of Physics, University of Sargodha, Sargodha, Punjab, Pakistan
[5]Department of Physics, Thal University Bhakkar, Bhakkar, Punjab, Pakistan
[6]Department of Hydrogen Technology, Rosenheim University of Applied Sciences, Burghausen Campus, 84489 Burghausen, Germany

DOI: https://doi.org/10.36348/sjet.2026.v11i08.003 | **Received:** 14.06.2026 | **Accepted:** 07.08.2026 | **Published:** 14.08.2026

***Corresponding author:** Rajab Abbas
Department of Materials Science and Engineering, Ghulam Ishaq Khan Institute of Engineering Sciences and Technology, Topi, Khyber Pakhtunkhwa, Pakistan

Abstract

Solid electrolytes are commonly designed using static descriptors such as crystallographic bottlenecks, vacancy concentrations, and migration barriers, yet emerging evidence shows that anion translation, rotation, vibration, and disorder can actively reorganize ionic energy landscapes. This review establishes a unified materials framework linking dynamic anion sublattices, cooperative ion migration, and metastable pathway engineering across lithium-, sodium-, proton-, and multivalent-ion conductors. A literature synthesis will compare sulfides, halides, oxyhalides, complex hydrides, solid acids, antiperovskites, and amorphous or partially crystalline electrolytes. Particular emphasis is placed on distinguishing independent hopping from correlated, concerted, paddle-wheel, and phonon-assisted transport; identifying when anion motion is causal rather than merely coincident; and determining how mixed-anion chemistry, defects, strain, mechanochemistry, quenching, and controlled amorphization stabilize transport-active configurations. Mode-resolved spectroscopy, neutron methods, solid-state nuclear magnetic resonance, total scattering, ab initio molecular dynamics, enhanced sampling, and machine-learned interatomic potentials are critically evaluated for resolving coupled sublattice dynamics across time and length scales. Quantitative structure–dynamics–transport relationships are proposed using conductivity, activation energy, correlation factors, rotational timescales, phonon characteristics, disorder metrics, and electrochemical stability. The review concludes with experimentally testable design rules and standardized reporting priorities for discovering room-temperature solid electrolytes that combine rapid ion conduction, metastable retention, interfacial compatibility, and device-level durability.

Keywords: Dynamic anion sublattices; Cooperative ion migration; Metastable pathway engineering; Mixed-anion solid electrolytes; Phonon-assisted transport; Superionic conductors.

1. INTRODUCTION

Solid electrolytes are central to safer, high-energy electrochemical storage, yet practical performance requires more than high ionic conductivity. An effective material must combine rapid ion transport, electronic insulation, electrochemical stability, processability and electrode contact. Sulfides are conductive and deformable but can be reactive; oxides are often stable yet rigid and difficult to densify; and halides offer oxidative stability but remain sensitive to composition, moisture, processing, and interfaces. Materials selection must therefore optimize transport, stability, mechanics, and manufacturability together.

Conventional discovery treats the host lattice as a static migration network. Bottleneck radius, lattice volume, vacancy concentration, site occupancy, pathway dimensionality, and activation energy remain useful descriptors. However, concerted migration shows that fast diffusion cannot always be reduced to independent hops (He *et al.,* 2017), while lattice-dynamics studies connect low-frequency vibrations with mobility and transport–stability trade-offs (Muy *et al.,* 2018). Time-averaged structures cannot represent transient coordination, bottleneck opening, anharmonic relaxation, interstitial states, or correlated rearrangements. Static calculations may therefore identify geometrically plausible pathways without establishing whether they are dynamically accessible.

A dynamic anion sublattice contains monatomic or polyatomic anions undergoing translation, rotation, libration, vibration, or collective reorientation on timescales relevant to ion migration. Translation shifts an anion's center; rotation changes orientation; libration is restricted oscillation; vibration changes internal bonds; collective motion couples framework units. These motions reshape instantaneous electrostatic potentials, coordination environments, bottleneck dimensions, and site energies. Anharmonic cation–anion coupling in sulfides can accelerate lithium diffusion by allowing the framework to participate in migration (Xu *et al.,* 2022).

Recent evidence establishes dynamic-sublattice control as a design strategy. In Li3YCl6-related halides, collective anion motion triggered a superionic transition, and halogen mixing produced room-temperature conductivities of 6.1 and 11 mS cm−1 (Liu *et al.,* 2024). Mechanochemically formed amorphous Li–Ta–Cl electrolytes reached 7.16 mS cm−1 with low stiffness, linking disorder, transport, and processability (Li *et al.,* 2023). Amorphous oxyhalides created connected Zr–O/Cl environments supporting rapid lithium transport (Zhang *et al.,* 2024). Dual-anion Na2O2–MCly glasses reached 2.0 mS cm−1 and enabled cycling (Lin *et al.,* 2025). In NaTaCl6, mechanically activated [TaCl6] rotation and structural disorder facilitated sodium diffusion, whereas the ordered niobium analogue remained poorly conducting (Li *et al.,* 2025).

Dynamic disorder is not universally beneficial. Microsecond machine-learning molecular dynamics found that PS4 rotation in crystalline Li7P3S11 weakly hindered lithium diffusion (Xu *et al.,* 2023). Temporal coincidence therefore cannot prove a paddle-wheel mechanism. Causality requires selective suppression or activation, isotope substitution, frequency shifts, or time-resolved correlations showing that anion motion changes cation displacement.

This review examines crystalline and disordered lithium-, sodium-, proton-, and multivalent-ion conductors. It connects anion chemistry, lattice dynamics, cooperative migration, metastable processing, and conductivity across halides, oxyhalides, sulfides, argyrodites, complex hydrides, solid acids, and antiperovskites. Its objectives are to distinguish causal from incidental anion motion, identify transferable dynamic descriptors, and determine how mechanochemistry, quenching, substitution, strain, and controlled amorphization stabilize transport-active configurations. It develops testable rules linking anion mass, charge, geometry, polarizability, disorder, and rotational freedom with migration topology, interfacial compatibility, and retention.

2. REVIEW METHODOLOGY AND EVIDENCE-SYNTHESIS FRAMEWORK

2.1. Literature-Search Protocol

A reproducible literature-search protocol was designed in accordance with PRISMA 2020 and PRISMA-S recommendations for transparent identification and reporting of evidence (Page *et al.,* 2021; Rethlefsen *et al.,* 2021). Web of Science Core Collection, Scopus, Dimensions, Crossref, and Google Scholar will be searched independently because their indexing scope, metadata structure, and document coverage are complementary. The search will cover January 2000 to July 2026, while studies published during 2020–2026 will receive detailed emphasis to capture the rapid expansion of dynamic solid-electrolyte research.

Search strings will combine controlled concepts and free-text variants using Boolean operators, phrase searching, truncation, and database-specific field codes. The core expression will connect solid-electrolyte terms with dynamic-mechanism and processing terms: ("solid electrolyte*" OR "superionic conductor*") AND ("dynamic anion sublattice*" OR "polyanion rotation" OR "anion reorientation" OR "paddle-wheel transport" OR "cooperative ion migration" OR "concerted ion migration" OR "phonon-assisted diffusion" OR "ion–phonon coupling" OR "mixed-anion electrolyte*" OR "metastable solid electrolyte*" OR "mechanochemical disorder" OR amorphization). Additional searches will use material-family names, including argyrodites, halides, oxyhalides, sulfides, complex hydrides, antiperovskites, solid acids, and sodium superionic conductors.

2.2. Eligibility, Classification, and Quality Assessment

Eligible evidence will comprise studies of inorganic solid electrolytes in crystalline, glassy, amorphous, nanocrystalline, or partially crystalline states when anion dynamics are investigated experimentally, computationally, or through a clearly testable combined approach. Lithium-, sodium-, proton-, fluoride-, oxide-, and selected multivalent-ion conductors will be considered, provided that the material performs an electrolyte function and the study examines anion translation, rotation, libration, vibration, collective

reorientation, or dynamically generated disorder. Mixed-anion halides, oxyhalides, sulfide-halides, argyrodites, complex hydrides, solid acids, antiperovskites, and related metastable conductors will be classified by mobile ion, anion chemistry, structural state, dimensionality, and proposed transport mechanism.

Liquid electrolytes, ionic liquids, gel systems, and conventional polymer electrolytes lacking a dynamic anionic framework will be excluded. Electrode materials will also be excluded unless electrolyte functionality is demonstrated through ionic conductivity, negligible electronic conductivity, or validated cell integration. Studies reporting only static structures, unvalidated bond-valence maps, or calculated migration barriers without dynamical analysis will remain eligible for background discussion but will not contribute to mechanism-level synthesis. Conference abstracts, patents, non-peer-reviewed claims, duplicate datasets, and articles lacking methodological detail will be excluded from quantitative comparison.

Evidence will be graded using a four-level hierarchy. Grade I will require direct experimental resolution of anion motion and ion transport through techniques such as neutron or synchrotron scattering, solid-state nuclear magnetic resonance, vibrational spectroscopy, and impedance measurements. Liu et al. (2024), for example, combined scattering and ab initio molecular dynamics to associate collective anion motion with the superionic transition in Li_3YCl_6. Grade II will include atomistic simulations validated against experimental structure, conductivity, spectroscopy, or temperature-dependent trends. Long-timescale machine-learning molecular dynamics will be accepted only when training accuracy, simulation size, duration, and transferability are reported; this is important because polyanion rotation may weakly hinder rather than promote diffusion in some thiophosphates (Xu *et al.,* 2023). Grade III will represent indirect mechanistic inference based on correlated changes in conductivity, disorder, phonon spectra, or rotational signatures. Grade IV will identify unverified conceptual attribution, including paddle-wheel or phonon-assisted labels assigned without time-resolved, perturbative, or correlation evidence. Conclusions will be weighted toward Grades I and II.

2.3. Data Extraction and Quantitative Synthesis

For each eligible study, a standardized extraction sheet will record composition, mobile-ion species, anion identity, crystal structure, space group, phase fraction, structural state, synthesis route, processing history, temperature, pressure, particle size, and density. Functional variables will include total, bulk, and grain-boundary conductivity; activation energy; tracer and collective diffusion coefficients; ionic transference number; electronic conductivity; and electrochemical stability. Processing details, including milling energy, annealing, quenching, substitution, and amorphization, will be retained because metastable transport can depend on preparation history.

Dynamic descriptors will include phonon frequency, linewidth, lifetime, anharmonicity, rotational correlation time, angular-jump distribution, anion mean-squared displacement, disorder parameters, site occupancies, and transition temperatures. Transport descriptors will include hopping frequency, residence time, jump length, van Hove functions, Haven ratio, correlation factor, string length, and the number of concertedly moving ions. Molecular-dynamics values will be extracted with simulation temperature, cell size, trajectory duration, force model, and extrapolation method because these choices affect calculated diffusivity (de Klerk *et al.,* 2018). Many-ion analyses will be prioritized where available, since higher-order correlations are frequent and cannot be represented adequately by independent-hopping models (López *et al.,* 2024).

Quantitative synthesis will use cross-family structure–dynamics–transport maps rather than rankings. Conductivity and diffusion data will be temperature-normalized, while crystalline, amorphous, and mixed-phase materials will be displayed separately. Bubble plots, correlation matrices, and evidence-weighted mechanism maps will relate anion chemistry and dynamic descriptors to activation energy, conductivity, and stability. Because measurement protocols differ substantially, pooled effect estimates will be avoided unless datasets are sufficiently comparable; otherwise, trends, uncertainty, missing variables, and contradictory evidence will be reported explicitly.

3. ANION-SUBLATTICE CHEMISTRY AND STRUCTURAL LANDSCAPE

3.1. Chemically Rigid and Dynamically Active Anion Frameworks

Anion chemistry governs both the static geometry and dynamic flexibility of solid-electrolyte frameworks. In monatomic oxide, sulfide, and halide sublattices, transport depends on anion charge, lattice volume, polarizability, and coordination topology. Density-functional calculations on face-centred-cubic frameworks showed that anion charge and lattice volume alter tetrahedral–octahedral site energetics and migration barriers (Xu *et al.,* 2020). Oxide lattices are generally strongly bonded and less deformable, whereas sulfide and halide frameworks are softer and more polarizable, permitting larger thermally activated fluctuations.

Polyatomic anions add rotational, librational, and internal vibrational degrees of freedom. In closo-borates, $B_{12}H_{12}^{2-}$ clusters generate structural, chemical, and dynamical frustration, producing many accessible interstitial sites and a flatter cation-energy landscape (Kweon *et al.,* 2017). Mixed monocarba-closo-borate anions suppress ordered phases and stabilize disordered fast-ion-conducting structures over broad temperature

ranges (Tang *et al.,* 2016). However, rotational freedom is not universally beneficial. Microsecond machine-learning molecular dynamics showed that rotating PS_4^{3-} units in crystalline $Li_7P_3S_{11}$ were weakly correlated with Li translation and slightly hindered diffusion, disproving an assumed room-temperature paddle-wheel effect (Xu *et al.,* 2023).

Recent halide studies provide stronger causal evidence. Collective chloride/bromide motion triggered the superionic transition in Li_3YCl_6-related compounds; $Li_3YCl_{4.5}Br_{1.5}$ and $Li_3GdCl_3Br_3$ reached 6.1 and 11 mS cm^{-1} at room temperature, respectively (Liu *et al.,* 2024). Mechanochemically disordered $NaTaCl_6$ delivered 3.3 mS cm^{-1} at 27 °C and an activation energy of 0.31 eV, whereas isostructural $NaNbCl_6$ reached only 0.01 mS cm^{-1} because $[TaCl_6]^-$ octahedra reoriented more readily (Li *et al.,* 2025). Polyanion substitution also produced a fourfold conductivity enhancement by inducing a dynamically disordered lithium sublattice (Guan *et al.,* 2026). Thus, useful frameworks require balanced polarizability, rotational freedom, connected migration topology, and retainable metastable disorder. These criteria distinguish genuinely transport-active anion dynamics from motions that are merely spectroscopic signatures of thermal disorder and do not measurably contribute to long-range ionic conduction.

Table 1: Quantitative examples linking anion-framework dynamics with ionic transport

Solid electrolyte	Anion framework	Dynamic feature	Room-temperature conductivity	Activation energy
$Li_3YCl_{4.5}Br_{1.5}$	Mixed monatomic Cl^-/Br^-	Collective anion motion and lowered superionic-transition temperature	6.1 mS cm^{-1}	Not specified
$Li_3GdCl_3Br_3$	Mixed monatomic Cl^-/Br^-	Dynamically activated mixed-halide framework	11 mS cm^{-1}	Not specified
$NaTaCl_6$	Octahedral $[TaCl_6]^-$	Facile octahedral rotation in a nanocrystalline framework	3.3 mS cm^{-1}	0.31 eV
$NaNbCl_6$	Octahedral $[NbCl_6]^-$	More ordered framework and restricted octahedral rotation	0.01 mS cm^{-1}	Not specified
Na_2O_2–MCl_γ	Amorphous dual O^{2-}/Cl^-	Mixed-anion coordination and disordered migration network	Up to 2.0 mS cm^{-1}	Composition-dependent

3.2. Mixed-Anion and Compositionally Complex Conductors

Mixed-anion design is not merely a compositional substitution strategy; it can reconstruct the local coordination landscape that governs carrier density, migration topology, lattice response, and phase stability. Oxyhalides provide the clearest evidence. $LiNbOCl_4$ and $LiTaOCl_4$ exhibit room-temperature conductivities of 10.4 and 12.4 mS cm^{-1}, respectively, despite being measured as cold-pressed powders, showing that O/Cl coordination can create highly connected Li-ion pathways without relying on a conventional close-packed halide lattice (Tanaka *et al.,* 2023). More recently, crystalline $Li_3Ta_3O_4Cl_{10}$ reached 13.7 mS cm^{-1} at 25 °C because corner-sharing oxygen and terminal chlorine form mixed-anion spiral chains and continuous tetrahedron-to-tetrahedron pathways (Zhao *et al.,* 2025). In amorphous $Li_3ZrCl_4O_{1.5}$, oxygen incorporation reorganized Zr–O/Cl polyhedra and lowered local transport barriers, yielding 1.35 ± 0.07 mS cm^{-1} (Zhang *et al.,* 2024). Dual-anion Na_2O_2–MCl_γ glasses similarly reached 2.0 mS cm^{-1}, where bridging and non-bridging oxygen species provided complementary structural functions rather than acting as simple vacancy dopants (Lin *et al.,* 2025).

Hydroxyhalides illustrate a less favourable regime: Br substitution in $Li_2OHCl_{1-x}Br_x$ modifies grain and grain-boundary resistances, but conductivity remains far below superionic oxyhalides, indicating that mixed anions do not automatically flatten site energies (Lee *et al.,* 2022). In sulfide–halide argyrodites, S^{2-}/X^- disorder redistributes Li-site energies and connects otherwise isolated diffusion cages; halide substitution and mixed Cl/Br occupancy therefore improve long-range transport through configurational connectivity, not lattice expansion alone (Kraft *et al.,* 2017; Adeli *et al.,* 2019; Morgan, 2021). Hydride–halide $LiBH_4$–LiBr–LiCl solid solutions stabilize the rotationally disordered hexagonal phase near room temperature, coupling framework reorientation with Li mobility (Gulino *et al.,* 2019). Oxynitride LiPON provides an amorphous counterpart, where nitrogen changes phosphate-network connectivity and Li coordination rather than simply increasing free volume (Lacivita *et al.,* 2018). Finally, mixed-polyanion NASICONs show that SiO_4/PO_4 distributions tune vacancy availability and migration-unit energetics; $Na_{3.4}Zr_2Si_{2.4}P_{0.6}O_{12}$ achieved approximately 0.165 S cm^{-1} at 473 K, matching large-scale kinetic Monte Carlo predictions (Deng *et al.,* 2022). Collectively, these systems demonstrate genuine cooperative effects when anion mixing simultaneously reshapes topology, disorder, dynamics, and defect thermodynamics. The decisive metric is therefore not average cell volume, but whether chemically heterogeneous coordination creates a percolating network of dynamically accessible states.

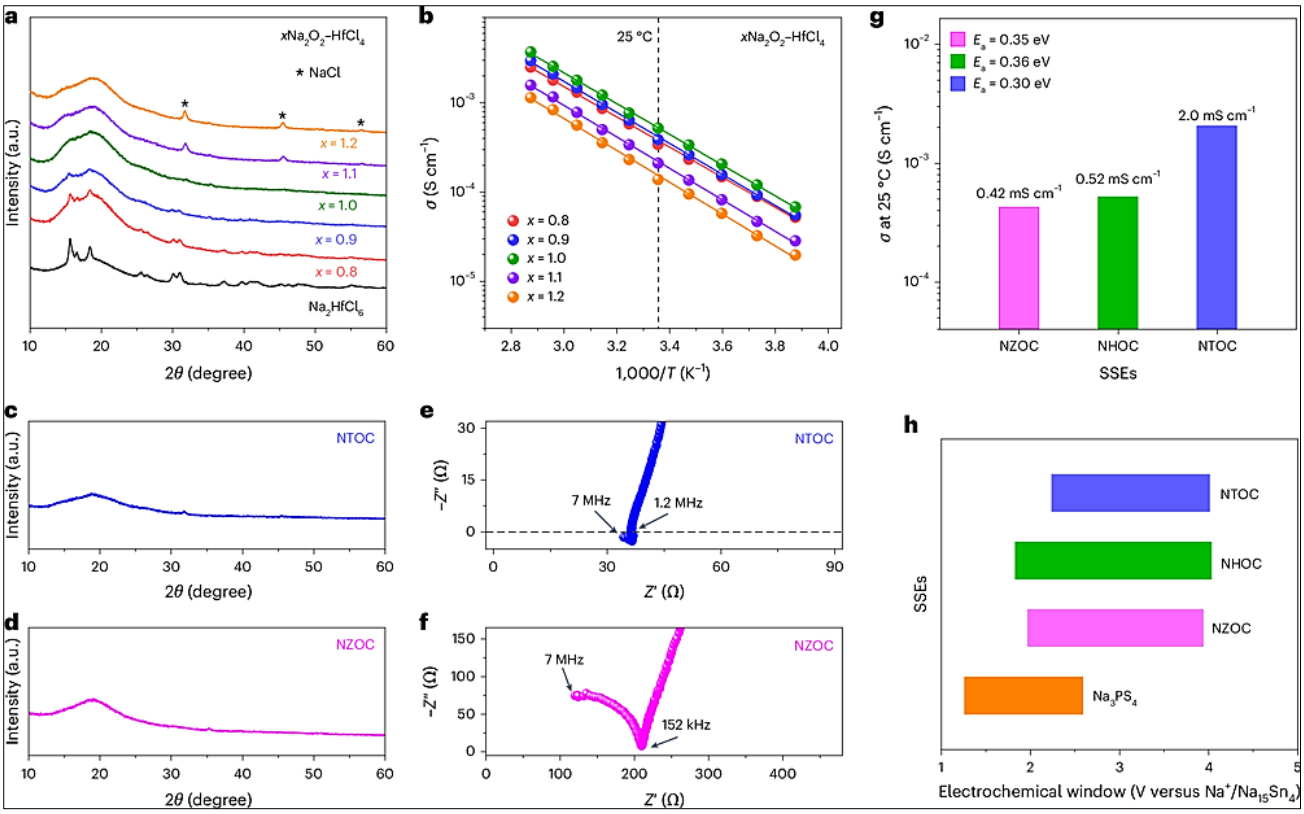

Figure 1: Mixed-Anion Synergy Beyond Defect Doping: Coordination Reconstruction, Dynamic Disorder, and Percolating Ion-Transport Networks

The published figure from Lin et al. compares temperature-dependent ionic conductivity, activation energy, impedance behaviour, and electrochemical stability of amorphous dual-anion Na_2O_2–MCl_γ electrolytes, where M represents Hf, Zr, or Ta. It demonstrates that oxygen and chlorine perform complementary structural functions, producing conductive amorphous networks rather than acting only through lattice expansion or vacancy generation

3.3. Crystalline Disorder, Amorphous States, and Metastable Polymorphs

Crystalline disorder must be separated into four physically distinct classes. Substitutional disorder occurs when chemically different ions share one crystallographic sublattice; in mixed-anion closo-borates, this geometric frustration suppresses ordered low-conductivity phases and stabilizes fast-ion states over a broad temperature range (Tang *et al.,* 2016). Occupational disorder describes partial or redistributed site populations. In Li_xScCl_{3+x}, tuning Li/Sc occupancy changed pathway connectivity and conductivity, whereas mechanochemical Li_3YCl_6 contains cation disorder and stacking faults that lower migration barriers; mild annealing reduces these defects and correspondingly alters transport (Liang *et al.,* 2020; Sebti *et al.,* 2022). Orientational disorder refers to statistically distributed polyanion orientations, while dynamic disorder requires time-dependent translational, rotational, or vibrational rearrangement during measurement. These states are related but not interchangeable: a diffraction-disordered solid may possess slow frozen disorder, whereas an average ordered structure may exhibit rapid local motion.

Amorphous electrolytes remove long-range periodicity but retain composition-dependent short- and medium-range coordination. Mechanochemically prepared Li–Ta–Cl glasses reached 7.16 mS cm^{-1} and a Young's modulus near 3 GPa, illustrating how disordered coordination can combine transport and mechanical compliance (Li *et al.,* 2023). Figure 2 shows the corresponding structure–property principle in $Li_3ZrCl_4O_{1.5}$: increasing the amorphous oxyhalide fraction reorganizes local Zr–O/Cl polyhedra, raises room-temperature conductivity to 1.35 ± 0.07 mS cm^{-1}, and lowers activation energy relative to crystalline Li_2ZrCl_6 (Zhang *et al.,* 2024). Amorphous xLi_2O–$TaCl_5$ compositions similarly reached 6.6 mS cm^{-1} at 25 °C and supported more than 2,400 cycles in a laboratory cell, confirming that disorder can remain electrochemically functional (Zhang *et al.,* 2023).

Nanocrystalline and amorphous–crystalline composites add interfacial pathways. Mechanochemical ZrO_2–Li_2ZrCl_6 networks increased Li-ion conductivity from 0.40 to 1.3 mS cm^{-1} at 30 °C through oxygen-substituted interfaces (Kwak *et al.,* 2023). Processing history is therefore a state variable: ball milling, quenching, and low-temperature annealing control defect density, crystallite size, stored strain, and structural relaxation. In $NaTaCl_6$, 15 h milling produced

a highly conducting amorphous state, while longer milling further reduced crystallinity (Li *et al.,* 2025). Metastability is beneficial only when kinetically trapped disorder remains connected, chemically stable, and reproducible; otherwise, relaxation or recrystallization can erase the transport advantage during prolonged operation and storage.

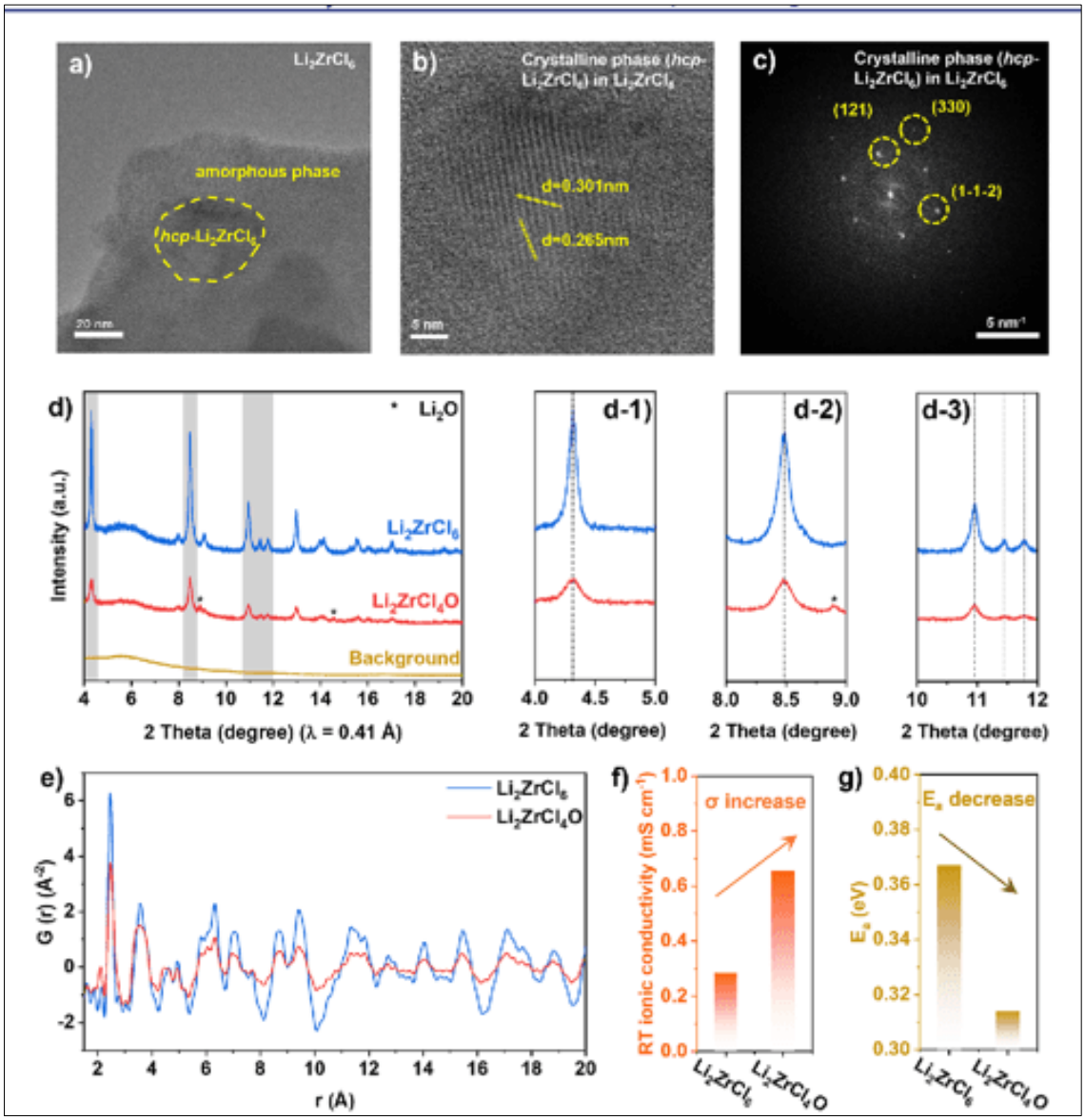

Figure 2: Disorder-Enabled Superionicity: From Crystalline Phase Disruption to Amorphous Oxyhalide Transport Networks

This published figure from Zhang et al. (2024) combines transmission electron microscopy, diffraction, pair-distribution-function analysis, ionic conductivity, and activation-energy comparisons for Li–Zr–Cl–O electrolytes. It shows that mechanochemical oxygen incorporation generates amorphous regions with reorganized Zr–O/Cl coordination, increasing conductivity relative to crystalline Li_2ZrCl_6. It is the most directly relevant published figure for explaining how amorphization and residual nanocrystallinity influence transport. For journal submission, reproduce it only under the publisher's permission conditions or prepare an original redrawn schematic with attribution.

4. DYNAMIC ANION SUBLATTICES: MOTIONS, PHONONS, AND ENERGY-LANDSCAPE FLUCTUATIONS

4.1. Translation, Rotation, Libration, and Vibration

Dynamic anion sublattices involve four distinguishable motions. Translation displaces an anion or polyanion centre of mass and can collectively reshape neighbouring cation sites. Rotation produces large angular reorientation, whereas libration is a restricted oscillation about an equilibrium orientation. Vibration changes internal bond lengths or framework coordinates, generating phonons from terahertz, sub-picosecond optical modes to slower, picosecond acoustic responses. Their amplitudes and correlation times determine

whether they merely broaden local structures or transiently modify migration barriers.

NMR provides quantitative separation of these processes. In Li_6PS_5X argyrodites, PS_4^{3-} rotational correlation rates approach 10^9 s^{-1}; the corresponding relaxation maxima occur near 223, 233, and 283 K for X = I, Br, and Cl, respectively (Hanghofer *et al.,* 2019). However, rapid rotation alone does not guarantee coupled transport. One-microsecond machine-learning molecular dynamics showed that $Li_{10}GeP_2S_{12}$, β-Li_3PS_4, Li_3ErCl_6, and Li_3YBr_6 exhibited only librational motion at 300 K, while selected PS_4^{3-} units in $Li_7P_3S_{11}$ completed approximately 120° rotations within 5–6 ps; these events were weakly correlated with Li hopping and slightly hindered overall diffusion (Xu *et al.,* 2023). Conversely, collective halogen motion in Li_3YCl_6-type electrolytes was directly associated with the superionic transition, showing that coherent framework displacement can be causally important (Liu *et al.,* 2024).

Frequency matching is therefore mechanistic rather than purely spectral. Coupling is expected when anion correlation times overlap cation residence or hopping times and when perturbing the anion mode changes conductivity. In closoborate $0.7Li(CB_9H_{10})$–$0.3Li(CB_{11}H_{12})$, NMR relaxation, impedance, and PFG-NMR yielded consistent activation behaviour across nanosecond-to-millisecond windows, supporting persistent coupled dynamics (Dorai *et al.,* 2024). Picosecond impedance measurements in $Li_{0.5}La_{0.5}TiO_3$ likewise tracked optical- and acoustic-phonon timescales, directly linking ultrafast lattice response to enhanced Li migration (Pham *et al.,* 2025). Accordingly, useful dynamic descriptors must combine frequency, amplitude, spatial coherence, and transport correlation. No single motion class is universally beneficial across all electrolyte chemistries. In table 2 The $Li_7P_3S_{11}$ values were obtained from microsecond-scale machine-learning molecular dynamics. The mixed-halide conductivity values were reported for compositions designed by controlling collective anion motion. $NaTaCl_6$ and $NaNbCl_6$ were evaluated under comparable processing conditions, enabling a direct quantitative comparison.

Table 2: Quantitative characteristics of anion motion in representative solid electrolytes

Solid electrolyte	Dominant anion motion	Dynamic descriptor	Ionic-transport properties
$Li_7P_3S_{11}$	PS_4^{3-} rotation	Approximately 120° rotation completed within 5–6 ps during 1 μs simulation at 300 K	Polyanion-rotation barrier: 0.60–0.68 eV
$Li_3YCl_{4.5}Br_{1.5}$	Collective Cl^-/Br^- motion	Mixed-halide motion lowers the superionic-transition temperature	Conductivity: 6.1 mS cm^{-1} at room temperature
$Li_3GdCl_3Br_3$	Collective Cl^-/Br^- motion	Dynamically active mixed-halide framework	Conductivity: 11 mS cm^{-1} at room temperature
$NaTaCl_6$	$[TaCl_6]^-$ octahedral reorientation	Pronounced rotation within a mechanochemically disordered structure	Conductivity: 3.3 mS cm^{-1} at 27 °C; activation energy: 0.31 eV
$NaNbCl_6$	Restricted $[NbCl_6]^-$ reorientation	More crystalline structure under the same milling conditions	Conductivity: 0.01 mS cm^{-1} at 27 °C; activation energy: 0.38 eV

Anion motion should be considered transport-promoting only when its timescale overlaps ion migration and experimental or computational perturbation demonstrates a corresponding conductivity change. The $Li_7P_3S_{11}$ case shows that fast polyanion rotation can remain weakly correlated—or even detrimental—to long-range ion diffusion.

4.2. Anharmonicity, Lattice Softness, and Phonon–Ion Coupling

Anharmonicity describes the nonlinear response of a lattice when atomic displacements extend beyond the harmonic approximation. In solid electrolytes, low-frequency modes of soft, polarizable frameworks can produce large-amplitude fluctuations that transiently widen migration bottlenecks, weaken mobile-ion coordination, and connect neighbouring sites. Comparative studies of lithium conductors associated lower Li-weighted phonon frequencies with faster transport, although the same soft bonding can reduce oxidative stability (Muy *et al.,* 2018). In Na_3PS_4–xSe_x, selenium substitution softened the lattice and shifted vibrational spectra, but descriptor performance depended on whether local, acoustic, or average phonon responses were considered (Krauskopf *et al.,* 2018).

Phonons modify migration through several coupled pathways. Framework displacements alter instantaneous electrostatic potentials and coordination numbers; anharmonic relaxation reduces the energy required to reach transition-state geometries; and collective modes can redistribute defect formation and site energies. Molecular dynamics of sulfide electrolytes showed that anharmonic cation–anion coupling pushes Li ions toward diffusion channels and lowers effective barriers (Xu *et al.,* 2022). In Li_3YCl_6, configurational disorder and selectively softened zone-boundary modes coupled host and Li motion across the superionic transition without destabilizing the chloride framework (Ahammed & Ertekin, 2024). Ta-doped garnet

$Li_{6.6}La_3Zr_{1.6}Ta_{0.4}O_{12}$ similarly exhibited lattice softening and enhanced anharmonic phonons associated with collective multi-ion migration (Kim *et al.,* 2025).

Not every soft or low-frequency mode promotes conduction. Productive modes must deform the bottleneck along the reaction coordinate, occur on timescales compatible with ion residence and hopping, and preserve network connectivity. Modes polarized away from the pathway may decorrelate successive hops, while excessive disorder can broaden site-energy distributions and create deep traps. In $Li_{10}GeP_2S_{12}$, progressive milling and amorphization decreased bulk conductivity, demonstrating that structural softening without coherent pathways can be detrimental (Schweiger *et al.,* 2022). Mode-selective experiments provide the strongest test: picosecond impedance measurements in $Li_{0.5}La_{0.5}TiO_3$ found that optical and acoustic phonon perturbations enhanced ultrafast Li migration, directly separating targeted lattice excitation from ordinary heating (Pham *et al.,* 2025). Consequently, phonon engineering should optimize mode symmetry, frequency, amplitude, anharmonicity, and spatial coherence rather than maximize lattice softness indiscriminately. This distinction is essential for converting spectroscopic correlations into transferable design rules for dynamically engineered solid electrolytes under operation.

4.3. Order–Disorder Transitions and Dynamic Phase Behaviour

Order–disorder transitions convert a localized ionic sublattice into a dynamically accessible network. In orientational transitions, polyatomic anions begin rapid rotation or reorientation; in translational transitions, mobile cations redistribute across partially occupied sites. Mixed-anion closo-borates demonstrate how configurational entropy can suppress low-conductivity ordered phases and stabilize rotationally disordered superionic structures near ambient temperature (Tang *et al.,* 2016). In lithium thiophosphates, entropy-driven stabilization of a high-temperature rotor phase at room temperature increased polyanion rotation and Li-ion diffusion, directly linking orientational disorder with transport (Zhang *et al.,* 2020). Collective halogen motion likewise controlled the superionic transition in Li_3YCl_6-related electrolytes, and mixed Cl/Br chemistry lowered the transition into the room-temperature regime (Liu *et al.,* 2024).

External variables shift these phase boundaries. Heating activates libration, reorientation, defect formation, and cation-site redistribution; $Na_4P_2S_6$ provides an example in which enhanced Na^+ mobility precedes and triggers formation of the fast-conducting rotor phase (Hogrefe *et al.,* 2025). Hydrostatic pressure can improve particle contact and modify phase fractions in sodium closo-hydroborates, producing conductivity enhancement, although excessive compression may restrict rotational free volume (Huang *et al.,* 2023). First-principles calculations predict that only 1–2% compressive strain can stabilize cation-disordered superionic phases of Cu_2Se and Li_2Se at ambient temperature by making tetrahedral and octahedral sites simultaneously accessible (Dumett Torres & Jain, 2018). Ultrafast terahertz fields can perturb optical and acoustic lattice modes on picosecond timescales, transiently enhancing Li migration without establishing a permanently transformed bulk phase (Pham *et al.,* 2025).

Metastable retention therefore requires kinetic arrest of a dynamically favourable structure. Ball milling stabilizes orientationally disordered $NaTaCl_6$ with 3.3 mS cm^{-1} conductivity at 27 °C, whereas annealing at 200 °C recrystallizes the material and lowers conductivity by two to three orders of magnitude (Li *et al.,* 2025). Polyanion substitution can similarly retain a disordered lithium sublattice near room temperature (Guan *et al.,* 2026).

5. COOPERATIVE ION MIGRATION: MECHANISMS AND QUANTITATIVE DESCRIPTORS

5.1. Independent Hopping versus Correlated Migration

Ion transport in solids spans isolated point-defect motion and collective many-ion rearrangement. In vacancy hopping, a lattice ion enters a neighbouring vacant site, whereas interstitial diffusion moves an excess ion between non-equilibrium sites. Interstitialcy, or knock-on, transport occurs when an interstitial displaces a lattice ion into the next available site, creating a propagating sequence. These mechanisms are distinct from concerted migration, in which several ions move within a correlated time window and lower the collective barrier through ion–ion interactions. In superionic conductors, therefore, the mobile-ion sublattice not only the host framework determines the accessible diffusion pathway (He *et al.,* 2017).

Table 3 summarizes quantitative evidence for this distinction. Ab initio molecular dynamics gave correlation factors of 3.0, 3.0, and 2.1 for $Li_{10}GeP_2S_{12}$, cubic $Li_7La_3Zr_2O_{12}$, and $Li_{1.3}Al_{0.3}Ti_{1.7}(PO_4)_3$, respectively, corresponding to approximately two to three correlated ions per event. Their concerted barriers were 0.20, 0.26, and 0.27 eV, substantially below the corresponding single-ion landscape barriers of 0.47, 0.58, and 0.49 eV (He *et al.,* 2017). In highly Al-doped LATP, paired M1–M2 migration becomes more favourable because excess Li populates higher-energy sites and Al-related trapping is reduced (Zhang *et al.,* 2020). Across a multi-family database containing millions of atomistic configurations, higher-order correlations involving more than two ions were more frequent than purely pairwise events; fast diffusion correlated more strongly with long hopping lengths and extended hopping spans than with hopping frequency alone (López *et al.,* 2024).

Concerted events can appear as synchronous nearest-neighbour hops, string-like displacement chains, or knock-on sequences in which one ion triggers the next. Local hops become long-range diffusion only when successive events connect across a percolating site network without repeated back-hopping or deep trapping. Van Hove distinct-correlation functions reveal whether a vacated site is rapidly occupied by another ion, while Haven ratios, collective-to-tracer diffusivity ratios, string-length distributions, and residence-time statistics quantify the degree and range of correlation. In Li_6PS_5Cl, lattice-bottleneck breathing produced an order-of-magnitude diffusivity increase, illustrating that framework dynamics can extend local correlated motion into a liquid-like transport network (Ding *et al.,* 2025). Mechanistic assignment should therefore combine defect topology, temporal correlation, network connectivity, and experimentally validated macroscopic transport coefficients.

Table 3: Quantitative descriptors of independent and cooperative ion migration

Material	Dominant migration event	Correlation factor	Concerted migration barrier	Single-ion landscape barrier
$Li_{10}GeP_2S_{12}$	Multi-ion concerted hopping	3.0	0.20 eV	0.47 eV
$Li_7La_3Zr_2O_{12}$	Cooperative tetrahedral–octahedral exchange	3.0	0.26 eV	0.58 eV
$Li_{1.3}Al_{0.3}Ti_{1.7}(PO_4)_3$	Paired M1–M2 migration	2.1	0.27 eV	0.49 eV
Li_6PS_5Cl	Correlated diffusion assisted by bottleneck breathing	Not reported as a single value	Not reported	Not reported

A correlation factor of 1 represents isolated single-ion diffusion, whereas values above 1 indicate positive many-ion correlation. The first three values were obtained from ab initio molecular-dynamics simulations at 900 K. In Li_6PS_5Cl, phonon-coupled bottleneck breathing produced an approximately order-of-magnitude increase in diffusivity, but the study did not report directly comparable scalar barrier or correlation-factor values.

5.2. Paddle-Wheel, Slingshot, and Phonon-Assisted Mechanisms

The conventional paddle-wheel model proposes that rotation of a polyatomic anion transiently opens a migration window and drives a neighbouring cation into a site. Figure 3 provides a clear test of this idea. In $NaTaCl_6$, $[TaCl_6]^-$ rotation enlarges the triangular Na^+ bottleneck by approximately 40%; during a 1 ps interval, a 27° ligand rotation coincides with a 3.14 Å Na^+ displacement. The corresponding Na^+ residence and joint cation–anion correlation times are 15.2 and 9.6 ps, respectively, compared with 23.4 and 16.3 ps in weakly reorienting $NaNbCl_6$ (Li *et al.,* 2025). These synchronized responses strongly support rotationally assisted hopping rather than simple coexistence of two independent motions.

Nevertheless, polyanion rotation should not automatically be labelled a paddle-wheel mechanism. One-microsecond simulations of $Li_7P_3S_{11}$ showed that complete PS_4^{3-} rotations occur much faster than long-range Li hopping and are weakly negative for diffusion, demonstrating that rotational frequency alone is insufficient (Xu *et al.,* 2023). Translationally assisted migration is broader: collective anion displacements, without complete rotation, can reshape site energies and trigger superionic transport, as observed when mixed Cl^-/Br^- motion lowered the transition temperature in Li_3YCl_6-derived conductors (Liu *et al.,* 2024). Framework breathing represents another limit, where phonon-driven changes in bottleneck area promote or suppress hopping. In LLTO, soft TiO_6 rotational distortions narrow pathways at moderate temperature, whereas anharmonic stabilization at higher temperature widens them (Malgope *et al.,* 2026).

The proposed proton-slingshot mechanism differs from a revolving paddle wheel. Nanosecond machine-learning molecular dynamics for CsH_2PO_4 and $CsHSO_4$ indicates that a proton is first carried by limited polyanion rotation and then propelled through aligned O–H bond reorientation to a recipient anion (Wang *et al.,* 2025). Because this study remains a preprint, the mechanism requires experimental confirmation. Causal coupling should therefore require: temporal synchronization between framework motion and ion displacement; spatial alignment with the migration coordinate; measurable bottleneck or barrier modulation; suppression or enhancement under constrained-motion, isotopic, compositional, or mode-selective perturbation; and agreement among conductivity, spectroscopy, scattering, and validated dynamics. Static structural similarity or simultaneous thermal activation alone cannot prove causation.

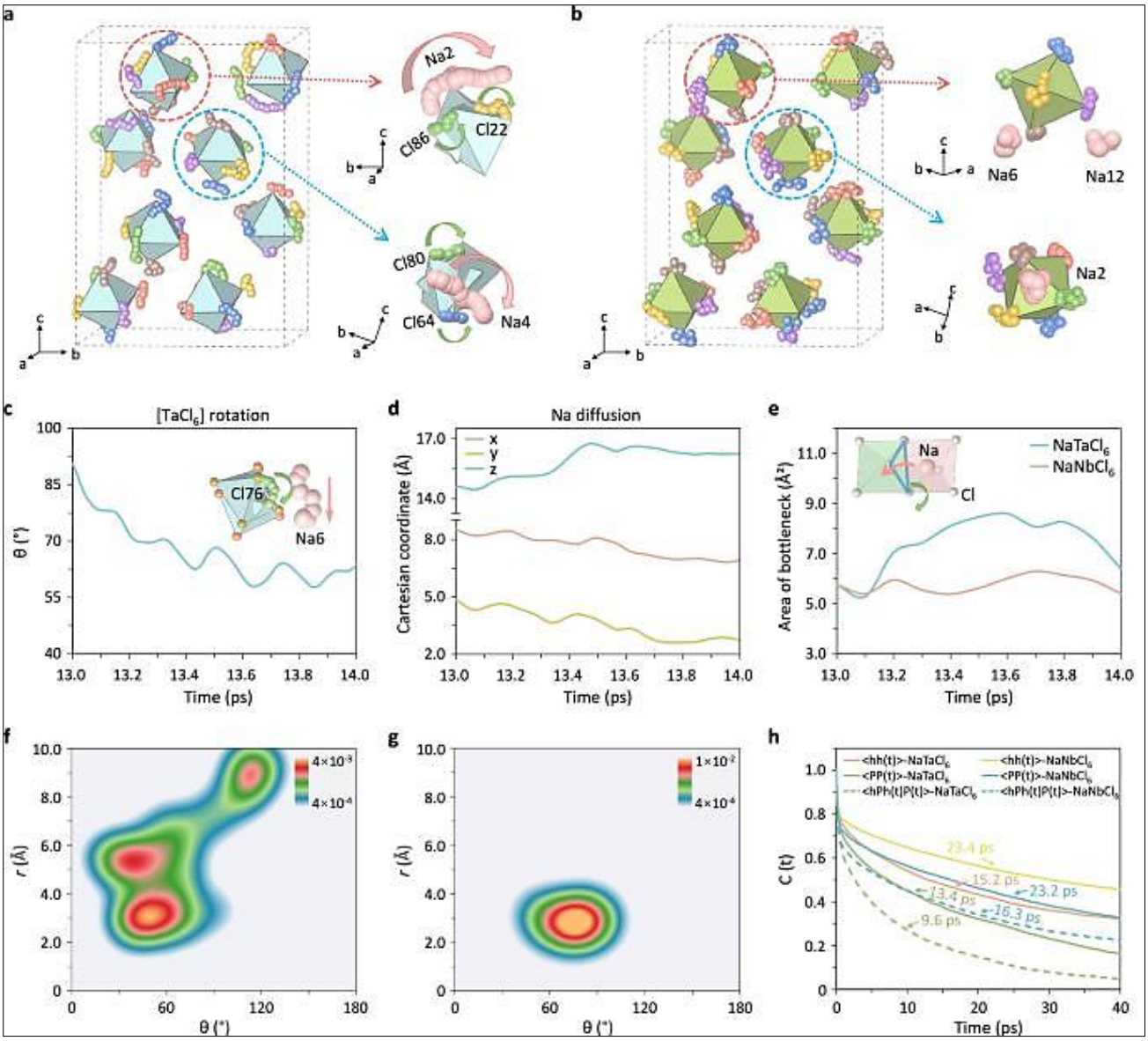

Figure 3: From Framework Rotation to Ion Escape: Direct Evidence for Paddle-Wheel-Coupled Bottleneck Opening

This published figure from Li et al. (2025) compares $NaTaCl_6$ with $NaNbCl_6$ using atomistic trajectories, polyanion-rotation angles, Na^+ displacement, bottleneck-area evolution, probability-density maps, and joint time-correlation functions. It shows that $[TaCl_6]^-$ rotation is synchronized with Na^+ hopping and temporarily enlarges the migration bottleneck, whereas restricted $[NbCl_6]^-$ motion produces weaker transport coupling.

5.3. Quantitative Identification of Cooperative Transport

Quantifying cooperative transport requires separating single-particle mobility from collective charge displacement. Tracer diffusivity, D*, follows the mean-squared displacement of individual ions, whereas the collective or charge diffusivity, Dσ, follows the squared displacement of the mobile-ion centre of mass. The Nernst–Einstein relation equates conductivity with D* only for uncorrelated carriers; therefore, conductivity–diffusivity deviations provide the first measure of correlation. The Haven ratio must be defined explicitly because the literature uses both D*/Dσ and its reciprocal (He *et al.,* 2018).

Figure 4 illustrates the next level of analysis. In LGPS, LLZO, and LATP, distinct van Hove functions reveal rapid occupation of sites vacated by neighbouring Li ions, while self-functions resolve individual jump lengths. At 900 K, He et al. (2017) obtained correlation factors of 3.0, 3.0, and 2.1, respectively, corresponding to approximately two to three ions participating in correlated events. Their concerted barriers, 0.20–0.27 eV, were substantially below single-ion landscape barriers of 0.47–0.58 eV.

No single scalar descriptor is sufficient. Displacement-covariance matrices identify positive,

negative, and directional coupling between ions; time-lagged correlations establish whether one displacement precedes another; and string analysis groups ions that exchange sites within a specified spatial and temporal window. Residence-time distributions distinguish persistent forward transport from rapid back-hopping, whereas the non-Gaussian parameter detects intermittent, spatially heterogeneous diffusion that is hidden by an averaged mean-squared displacement. Large-scale analysis further indicates that higher-order correlations are widespread and that long hopping spans can be more diagnostic of fast transport than hopping frequency alone (López *et al.,* 2024).

Thermodynamic descriptors provide complementary information. Migration entropy, obtained from the Arrhenius prefactor within a transition-state model, reflects the number of accessible configurations and vibrational changes at the saddle point. Activation volume, derived from the pressure dependence of conductivity or diffusivity, tests whether the transition state requires expansion. Mode-projected displacements identify phonons aligned with migration coordinates, while time-lagged cation–anion correlations determine whether framework motion drives, follows, or merely accompanies hopping (Huang *et al.,* 2023; Li *et al.,* 2025; Malgope *et al.,* 2026). Robust identification should combine conductivity, tracer diffusion, collective statistics, pathway topology, and uncertainty-aware trajectory analysis. All descriptors require matched temperatures, timescales, and compositions.

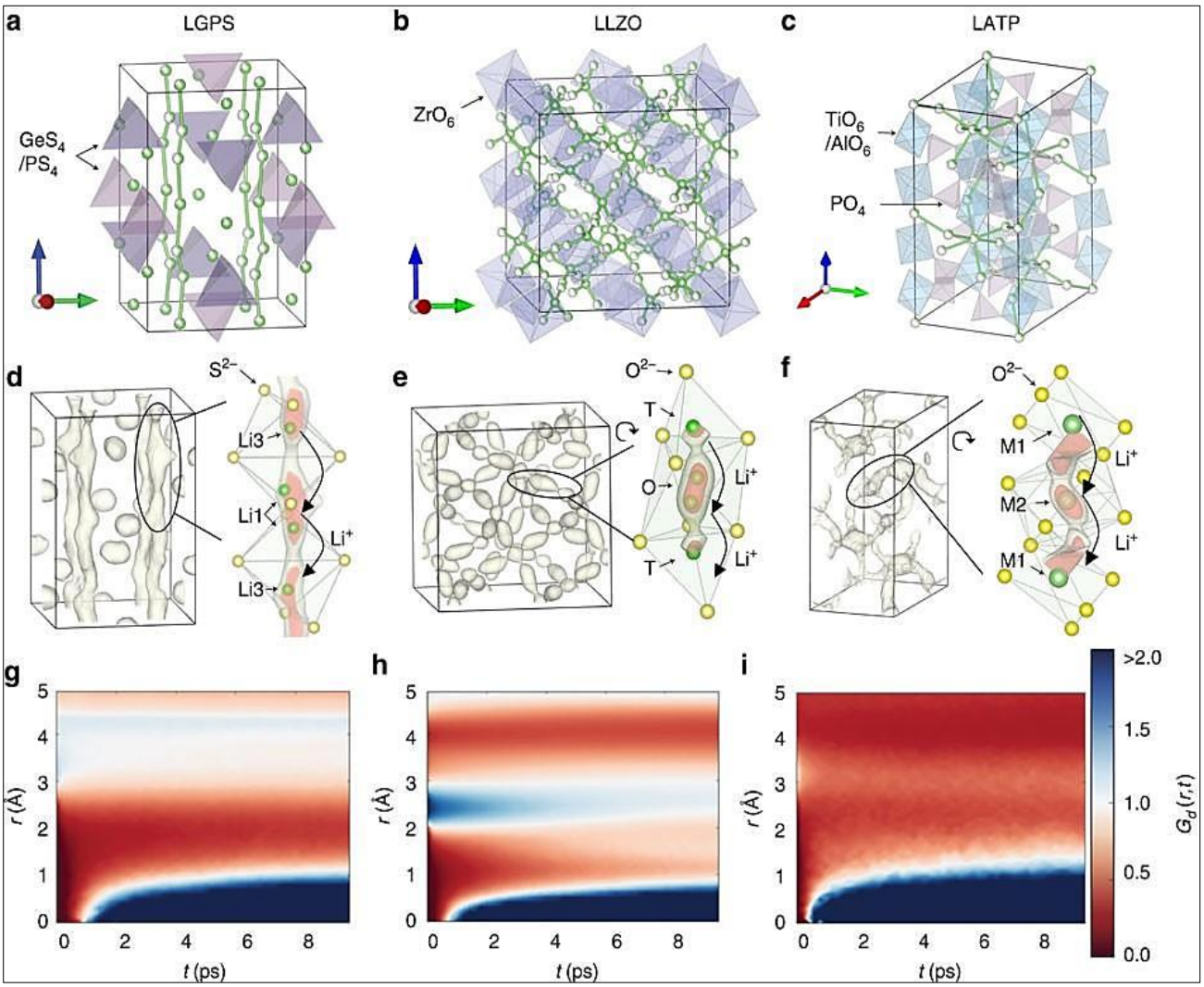

Figure 4: Beyond Mean-Squared Displacement: Van Hove Correlations and Many-Ion Signatures of Cooperative Diffusion

The displayed published figure from He *et al.,* (2017; original Figure 2) combines lithium probability-density distributions and van Hove correlation functions for $Li_{10}GeP_2S_{12}$, $Li_7La_3Zr_2O_{12}$, and $Li_{1.3}Al_{0.3}Ti_{1.7}(PO_4)_3$. The spatial-density panels identify connected migration channels, while the time-dependent van Hove functions reveal correlated occupation of sites vacated by neighbouring ions. The article is distributed under a CC BY 4.0 licence and may be reproduced with complete attribution.

6. METASTABLE PATHWAY ENGINEERING THROUGH SYNTHESIS AND PROCESSING

6.1. Mechanochemistry and Controlled Amorphization

Mechanochemistry drives solid-electrolyte formation through repeated fracture, cold welding, interfacial renewal, and highly localized impact events. Milling frequency, rotational speed, ball size, ball-to-powder ratio, step duration, and total treatment time collectively determine collision energy and energy dose. A 2026 orthogonal-design study of halide electrolytes identified the ball-to-precursor mass ratio, milling-step duration, and milling frequency as the parameters exerting the strongest influence on ionic conductivity, confirming that nominal milling time alone is an inadequate process descriptor (Beltran *et al.,* 2026). High ball-to-powder ratios increase collision frequency and contact renewal, but excessive impact energy can promote agglomeration, contamination, overheating, or parasitic reactions.

Mechanical energy is partitioned among heat, particle-size reduction, lattice strain, defects, stacking faults, and amorphous-region formation. Mechanochemical Li_3YCl_6 contains cation disorder and stacking faults that assist Li-ion transport, whereas annealing reduces these defects and modifies conductivity (Sebti *et al.,* 2022). In amorphous Li–Ta–Cl electrolytes, optimized milling generated disordered coordination environments and room-temperature conductivities up to 7.16 mS cm^{-1} (Li *et al.,* 2023). Similarly, 15 h milling produced poorly crystalline $NaTaCl_6$ with 3.3 mS cm^{-1} conductivity; post-annealing at 200 °C sharpened diffraction peaks and decreased conductivity by two to three orders of magnitude, linking retained disorder with dynamic $[TaCl_6]^-$ reorientation (Li *et al.,* 2025).

Beneficial amorphization is nevertheless composition- and dose-dependent. For $Li_{1.44}ZrCl_4N_{0.48}$, conductivity increased from 4.07×10^{-4} S cm^{-1} after 1 h to 3.21×10^{-3} S cm^{-1} after 24 h, but declined after 48–72 h as short-range ordering and agglomeration developed (Butenko *et al.,* 2026). Conversely, progressive amorphization of $Li_{10}GeP_2S_{12}$ disrupted connected diffusion pathways and reduced conductivity (Schweiger *et al.,* 2022). Controlled mechanochemistry must therefore target an optimal metastable window: sufficient disorder to activate flexible anion environments and percolating pathways, but insufficient energy to cause decomposition, impurity formation, contamination, or irreversible network collapse during subsequent storage and operation.

6.2. Thermal, Pressure, and Field-Assisted Pathway Control

Thermal, mechanical, and field-assisted processing can redirect solid-state reactions by altering nucleation barriers, diffusion lengths, defect populations, and cooling rates. Rapid melt quenching suppresses long-range ordering, whereas subsequent annealing or controlled recrystallization can isolate conductive metastable states before equilibrium competitors form. In $NaNbOCl_4$ and $NaTaOCl_4$, sub-second quenching fragmented Nb–Cl connectivity, increased Nb–O coordination, and generated coupled short- and long-range disorder; room-temperature conductivities reached 1.51 and 7.2 mS cm^{-1}, respectively (Ma *et al.,* 2026). Controlled recrystallization is equally trajectory-dependent. Mechanochemically amorphized LLZTO nucleated cubic garnet near 350 °C and delivered 1.8×10^{-4} S cm^{-1} after 500 °C for 2 h, whereas crystallizing the powder before densification produced only 4.2×10^{-7} S cm^{-1} under the same heat treatment (Kwon *et al.,* 2025).

Low-temperature topochemical conversion can access frameworks unavailable through direct equilibrium synthesis. Chemical fluorination at 200 °C transformed TlF into a cubic anti-α-CuBr-type phase containing intrinsic fluoride vacancies; the material exhibited 4.3 mS cm^{-1} at 398 K and an activation energy of 0.30 eV (Tani *et al.,* 2025). As summarized in Table 4, pressure can likewise create persistent polymorphs rather than merely improve pellet contact. Pressing $Na_2B_{10}H_{10}$:$Na_2B_{12}H_{12}$ mixtures between 97.5 and 2080 MPa increased the body-centred-cubic fraction and raised room-temperature conductivity from 2×10^{-4} to approximately 1×10^{-3} S cm^{-1} for the 1:1 composition (Huang *et al.,* 2023).

Strain and confinement reshape local energy landscapes without changing bulk composition. NBT–MgO nanopillar films developed interphase tensile strain approaching +2% and achieved 3×10^{-3} S cm^{-1} at 400 °C, over an order of magnitude above unstrained NBT (Huo *et al.,* 2024). Nanoconfined $LiBH_4/SiO_2$ reached 0.1 mS cm^{-1} at room temperature by stabilizing a mobile interfacial fraction (Lefevr *et al.,* 2018). Microwave crystallization doubled LAGP conductivity relative to conventional heating, while ultrafast high-temperature sintering completed crystallization and densification within 180 s, demonstrating that heating rate can decouple nucleation from grain growth (Mahmoud *et al.,* 2016; Curcio *et al.,* 2022). Overall, processing trajectory must be treated as a materials descriptor because identical compositions can occupy different metastable energy landscapes, phase fractions, and transport networks during synthesis, cooling, and subsequent operation.

Table 4: Quantitative effects of non-equilibrium processing on ionic transport

Processing strategy	Solid electrolyte	Quantitative transport outcome
Rapid quenching	$NaNbOCl_4$	1.51 mS cm^{-1} at room temperature
Rapid quenching	$NaTaOCl_4$	7.2 mS cm^{-1} at room temperature
Controlled recrystallization	Amorphous LLZTO	1.8×10^{-4} S cm^{-1} at 25 °C
Crystallization before densification	LLZTO	4.2×10^{-7} S cm^{-1} at 25 °C
Topochemical fluorination	TlF	4.3 mS cm^{-1} at 398 K; activation energy: 0.30 eV
Pressure-induced transformation	$Na_2B_{10}H_{10}$–$Na_2B_{12}H_{12}$	Conductivity increased from approximately 2×10^{-4} to 1×10^{-3} S cm^{-1} at room temperature
Interfacial strain engineering	NBT–MgO nanopillar film	3×10^{-3} S cm^{-1} at 400 °C; more than tenfold enhancement
Dimensional confinement	$LiBH_4/SiO_2$	Approximately 0.1 mS cm^{-1} at room temperature
Microwave crystallization	LAGP glass-ceramic	2.77×10^{-4} S cm^{-1}, compared with 1.30×10^{-4} S cm^{-1} after conventional processing
Ultrafast high-temperature processing	LAGP glass-ceramic	1.15×10^{-4} S cm^{-1} after crystallization and sintering within 180 s

The rapid-quenching oxyhalides reached 1.51 and 7.2 mS cm^{-1}, while changing the LLZTO processing sequence produced a conductivity difference of more than two orders of magnitude. Topochemically converted TlF showed 4.3 mS cm^{-1} at 398 K, and strain-engineered NBT–MgO films reached 0.003 S cm^{-1} at 400 °C. Ultrafast processing crystallized and sintered LAGP within 180 s, yielding 1.15×10^{-4} S cm^{-1}.

6.3. Chemical Stabilization of Transport-Active States

Chemical stabilization aims to preserve transport-active disorder without sacrificing electrochemical or structural integrity. Aliovalent substitution changes both carrier concentration and site-energy topology. In $Li_{5.35}Ca_{0.1}PS_{4.5}Cl_{1.55}$, Ca^{2+} substitution on Li^+ sites generated vacancies and produced 10.2 mS cm^{-1} room-temperature conductivity; however, the response depended on pellet compression and grain-boundary transport (Adeli *et al.,* 2021). In $Li_{6+x}P_{1-x}Si_xS_5Br$, Si^{4+} substitution tripled conductivity by populating intercage T4 sites and flattening the Li-energy landscape, rather than merely adding carriers (Schwietert *et al.,* 2024). Excess substitution can nevertheless narrow electrochemical stability, demonstrating that defect concentration must be optimized rather than maximized.

Mixed-anion incorporation can stabilize dynamically disordered phases through compositional frustration. Mixing 1-$CB_9H_{10}^-$ and $CB_{11}H_{12}^-$ suppressed ordered closo-borate phases and retained fast-ion-conducting solid solutions from subambient to elevated temperatures (Tang *et al.,* 2016). In mixed Cl^-/Br^- halides, compositional tuning lowered the collective-anion-motion transition into the room-temperature regime (Liu *et al.,* 2024). Dual-anion Na_2O_2–MCl_γ glasses further combined up to 2.0 mS cm^{-1} conductivity with mechanically compliant amorphous networks, showing that anion mixing can reconstruct coordination and connectivity beyond simple vacancy creation (Lin *et al.,* 2025).

High-entropy strategies extend this principle by distributing several cations and anions across broad local environments. A high-entropy amorphous oxyhalide, $Li_{1.6}Ta(PSiB)_{0.15}O_{1.65}Cl_5Br_{0.1}$, reached 7.1 mS cm^{-1} at 25 °C while improving electrochemical stability through multication mixing, mixed-anion coordination, and amorphous-phase retention (Song *et al.,* 2025). Yet configurational complexity may also cause segregation or batch variability. Annealing disordered $NaTaCl_6$ at 200 °C recrystallized the framework and reduced conductivity by two to three orders of magnitude, confirming that chemical design and processing history are inseparable (Li *et al.,* 2025). Reproducible stabilization therefore requires reporting precursor purity, substitution limits, milling energy, annealing history, density, aging time, and conductivity after thermal cycling. Long-term value should be judged by phase-retention lifetime and conductivity stability, not only the highest initial conductivity.

7. MULTISCALE VALIDATION AND TRANSLATION TO ELECTROCHEMICAL PERFORMANCE

7.1. Experimental Resolution of Dynamic Transport

Experimental validation of dynamic ion transport requires techniques that resolve energy, time, and length scales. Inelastic neutron scattering (INS) measures phonon densities of states and mode energies, making it suitable for identifying framework vibrations and anharmonic changes. Quasielastic neutron scattering (QENS), by contrast, detects stochastic motion through quasielastic broadening and can extract jump lengths, residence times, diffusion coefficients, and activation energies on picosecond-to-nanosecond and ångström scales. Combined INS–QENS analysis of BaH_2 separated hydride vibrations from vacancy-mediated diffusion and showed that the high-temperature phase

supports 3.1 Å jumps with reduced residence times and barriers (Novak *et al.,* 2022).

Solid-state NMR complements neutron methods by probing element-specific local environments and motion over broader windows. Spin–lattice relaxation and line narrowing quantify local hopping or polyanion reorientation, whereas pulsed-field-gradient NMR measures long-range self-diffusion. In Li_6PS_5X, ^{31}P relaxation resolved PS_4^{3-} rotational dynamics (Hanghofer *et al.,* 2019); combining relaxation, pulsed-field-gradient NMR, and impedance in closo-borates linked nanosecond local fluctuations with millisecond-scale conduction (Dorai *et al.,* 2024). Raman and infrared spectroscopy track bond-specific vibrations, symmetry changes, and disorder, while terahertz methods access low-frequency collective modes. Picosecond-resolved impedance in $Li_{0.5}La_{0.5}TiO_3$ linked transient conductivity changes with optical and acoustic phonon timescales (Pham *et al.,* 2025).

Structural and electrochemical measurements must establish whether these dynamics persist in functional materials. Synchrotron diffraction resolves phase fractions, strain, and site occupancy, whereas total-scattering pair-distribution-function analysis reconstructs short-range order in glasses and amorphous electrolytes. For $Li_3ZrCl_4O_{1.5}$, X-ray absorption, PDF analysis, and reverse Monte Carlo modelling identified transport-relevant amorphous Zr–O/Cl coordination (Zhang *et al.,* 2024). Impedance spectroscopy supplies conductivity and relaxation responses but cannot independently assign microscopic mechanisms. Operando synchrotron microdiffraction can map lattice parameters and grain orientation during cycling, linking electrolyte behaviour with evolving electrodes and interfaces (Jacquet *et al.,* 2025). Robust validation therefore requires multimodal agreement across spectroscopy, scattering, electrochemistry, and operando imaging.

7.2. Atomistic Modelling and Data-Assisted Discovery

Atomistic modelling converts static structural hypotheses into testable transport mechanisms. Density-functional theory (DFT) establishes phase energies, defect formation energies, bonding and relaxed migration geometries, while nudged-elastic-band calculations estimate minimum-energy barriers. Harmonic and anharmonic phonon calculations identify unstable, low-frequency or mode-specific framework displacements that may couple to mobile ions. Ab initio molecular dynamics (AIMD) resolves diffusion without an empirical force field, but its typical picosecond duration often requires elevated temperatures, making rare events, disorder transitions and room-temperature extrapolation uncertain (He *et al.,* 2018; Xu *et al.,* 2023). Enhanced-sampling approaches, including metadynamics, umbrella sampling and accelerated dynamics, can reconstruct free-energy surfaces and transition pathways, although conclusions depend strongly on collective-variable choice and valid reweighting.

Figure 5 illustrates the gain obtained with machine-learned interatomic potentials (MLIPs). Xu et al. (2023) trained moment-tensor potentials on DFT energies and forces from 1,800 configurations per electrolyte and extended simulations to 1 μs at 300 K. For $Li_7P_3S_{11}$, the calculated diffusion coefficient was 1.40×10^{-7} cm² s⁻¹ and conductivity was 14.96 mS cm⁻¹, close to experimental values of 11.6–17 mS cm⁻¹. The same trajectories captured rare PS_4^{3-} rotations that shorter AIMD could not observe and exposed non-Arrhenius transport in Li_3ErCl_6. Large-scale MLIP simulations of Li_6PS_5Cl subsequently required 25 ns and a 6,500-atom supercell to converge conductivity within 10%, demonstrating that both simulation length and system size affect mechanistic reliability (Lee *et al.,* 2024).

Data-assisted discovery now extends beyond individual materials. The LiTraj resource contains 13,000 percolation labels, 122,000 migration barriers and 1,700 DFT migration trajectories; fine-tuned universal MLIPs approached DFT accuracy for pathway screening (Dembitskiy *et al.,* 2025). Active-learning and transfer-learning workflows can reduce reference-data requirements, while model distillation has produced lightweight potentials hundreds of times faster than their teacher models (Zhang *et al.,* 2026).

Predicted mechanisms should nevertheless be accepted only after uncertainty assessment. Validation must include independent energy, force and stress errors; equation-of-state and phonon tests; defect and migration-barrier benchmarks; stable trajectories outside the training temperatures; ensemble-based extrapolation detection; finite-size and time-convergence analysis; and comparison with experimental conductivity, activation energy, scattering or spectroscopy. Agreement with training data alone does not establish transferable transport physics.

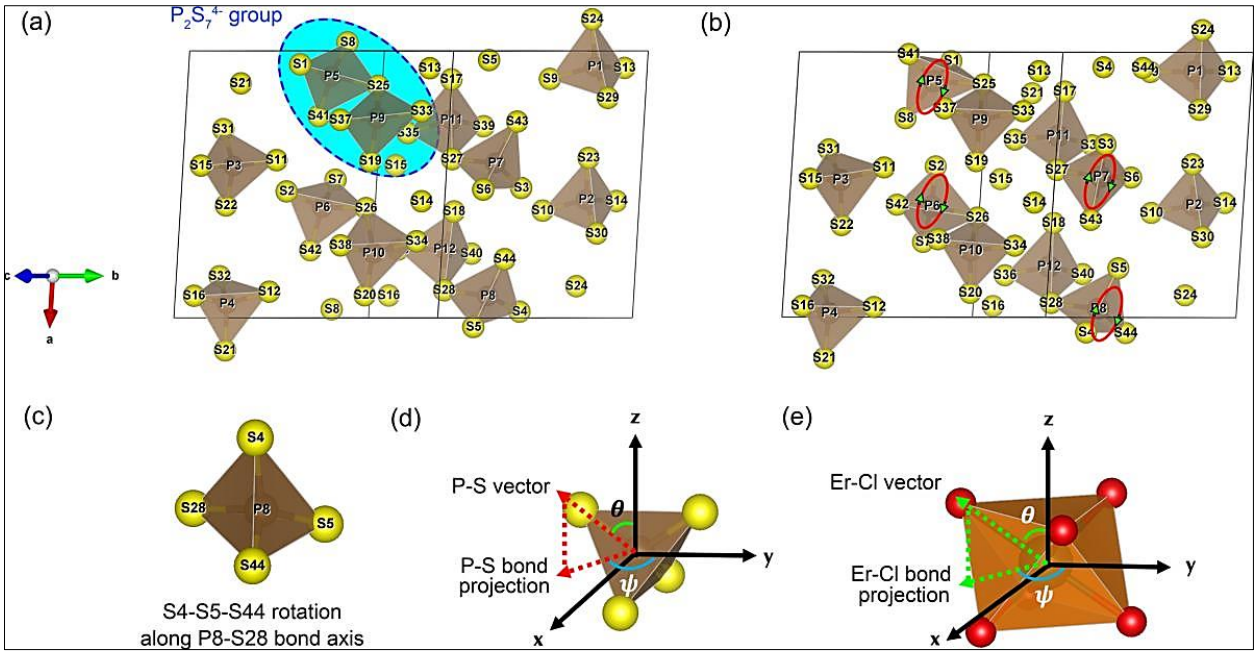

Figure 5: Bridging Quantum Accuracy and Realistic Transport Timescales: Machine-Learned Molecular Dynamics of Rare Anion and Ion-Migration Events

The published figure from Xu *et al.,* (2023) shows the $Li_7P_3S_{11}$ structure used for microsecond-scale machine-learning molecular dynamics, identifies the dynamically active $P_2S_7^{4-}$ units, and defines angular coordinates for tracking PS_4^{3-} rotation. The complete study connects DFT-generated training configurations with 1 μs simulations, room-temperature Li trajectories, free-energy surfaces and time-resolved anion–cation correlations. It therefore illustrates how machine-learned potentials can reveal rare dynamic events inaccessible to conventional short AIMD trajectories. The article is licensed under CC BY 4.0, permitting reproduction or adaptation with appropriate attribution and disclosure of modifications.

7.3. From Intrinsic Conductivity to Device-Relevant Performance

Intrinsic ionic conductivity becomes device-relevant only when transport is preserved across grains, interfaces, and processing-induced defects. Bulk conductivity describes ion motion inside crystallites, grain-boundary conductivity reflects intergranular barriers, and total conductivity combines both contributions. These values should be measured under standardized temperature, density, thickness, pressure, electrode geometry, frequency range, and equivalent-circuit criteria. LLTO illustrates the distinction: its room-temperature bulk conductivity is approximately 1.0×10^{-3} S cm^{-1}, whereas grain-boundary and total conductivities are about 7.5×10^{-5} and 7×10^{-5} S cm^{-1}, respectively, because reconstructed boundaries impede Li transport (Lee *et al.,* 2023). Interlaboratory benchmarking shows that pressing conditions, cell assembly, and analysis protocols create variability even for nominally identical Li_6PS_5Cl cells (Puls *et al.,* 2024).

High ionic conductivity is insufficient if electronic leakage, chemical decomposition, or poor mechanics destabilize the cell. Operando neutron profiling showed internal lithium deposition in LLZO and amorphous Li_3PS_4, linking finite electronic conductivity with filament formation, while electronically insulating LiPON resisted deposition (Han *et al.,* 2019). Grain boundaries can also accumulate electrons during plating and become preferred dendrite-nucleation sites (Zhu *et al.,* 2023). Mechanical deformability must preserve interparticle contact without enabling fracture or creep. Amorphous Li–Ta–Cl electrolytes combine conductivity up to 7.16 mS cm^{-1} with a Young's modulus near 3 GPa, improving contact with rigid high-nickel cathode particles (Li *et al.,* 2023).

Dynamic and metastable structures must survive pelletization, electrode contact, electric fields, and prolonged cycling. Disorder-driven LLZTO retained interparticle connectivity during mild crystallization and delivered 1.8×10^{-4} S cm^{-1} at 25 °C (Kwon *et al.,* 2025). Amorphous xLi_2O–$TaCl_5$ electrolytes maintained functional transport for more than 2,400 cycles, demonstrating that metastability can remain device-compatible when structural relaxation and interfacial reactions are controlled (Zhang *et al.,* 2023). Validation should report structure, electronic conductivity, pressure-dependent impedance, interface resistance, current density, and conductivity retention after cycling.

8. CONCLUSION

This review establishes that next-generation solid electrolytes cannot be designed from static crystal structures, migration bottlenecks, or activation barriers alone. Fast ionic conduction emerges from a coupled landscape in which anion chemistry, lattice softness,

structural disorder, vibrations, and many-ion correlations reshape migration pathways. Evidence from halide electrolytes shows that tuning collective anion motion can lower superionic transition temperatures and produce room-temperature conductivities of 6.1 to 11 mS cm^{-1} (Liu *et al.,* 2024). Likewise, mechanically activated $NaTaCl_6$ reaches 3.3 mS cm^{-1} because $[TaCl_6]^-$ reorientation transiently enlarges sodium migration bottlenecks, whereas less dynamic $NaNbCl_6$ remains poorly conducting (Li *et al.,* 2025).

The literature demonstrates that anion motion is not intrinsically beneficial. Microsecond machine-learning molecular dynamics revealed that PS_4^{3-} rotation in $Li_7P_3S_{11}$ is weakly correlated with lithium hopping and can slightly hinder diffusion (Xu *et al.,* 2023). Mechanistic assignments must therefore distinguish causal coupling from simultaneous thermal activation by combining time-resolved correlations, constrained-motion calculations, isotope or compositional perturbations, mode-selective spectroscopy, and conductivity measurements. Cooperative migration should similarly be evaluated using collective diffusivity, Haven ratios, van Hove functions, displacement covariance, string statistics, and residence-time distributions rather than single-particle mean-squared displacement alone.

Mixed-anion chemistry and metastable processing provide routes for stabilizing transport-active energy landscapes. Dual-anion amorphous sodium oxychlorides and lithium oxychlorides demonstrate that chemically heterogeneous coordination can combine high conductivity with mechanical compliance and prolonged cell operation (Lin *et al.,* 2025; Zhang *et al.,* 2023). However, beneficial disorder occupies a finite processing window: excessive milling, uncontrolled amorphization, impurity generation, or recrystallization can destroy percolating networks and erase dynamic advantages. Processing history must therefore be treated as a materials descriptor.

Future progress requires integration of operando scattering, spectroscopy, solid-state NMR, impedance, atomistic simulation, and machine-learned potentials. Models must report uncertainty, finite-size convergence, temperature transferability, and experimental validation. Candidate electrolytes should be judged by total conductivity, electronic leakage, interface resistance, mechanical integrity, phase-retention lifetime, and reproducible cell performance. Standardized reporting and shared datasets are essential because interlaboratory assembly differences can dominate measured outcomes (Puls *et al.,* 2024). Dynamic anion-sublattice engineering will become transformative only when microscopic transport mechanisms remain stable, scalable, and functional under realistic electrochemical operation.

REFERENCES

- Adeli, P., Bazak, J. D., Huq, A., Goward, G. R., & Nazar, L. F. (2021). Influence of aliovalent cation substitution and mechanical compression on Li-ion conductivity and diffusivity in argyrodite solid electrolytes. *Chemistry of Materials, 33*(1), 146–157. DOI: 10.1021/acs.chemmater.0c03090
- Adeli, P., Bazak, J. D., Park, K. H., Kochetkov, I., Huq, A., Goward, G. R., & Nazar, L. F. (2019). Boosting solid-state diffusivity and conductivity in lithium superionic argyrodites by halide substitution. *Angewandte Chemie International Edition, 58*(26), 8681–8686. DOI: 10.1002/anie.201814222
- Beltran, M., Wang, B., Tan, Y., Choi, J., Lee, D., & Su, L. (2026). Mechanochemistry-driven optimization of halide-based solid-state electrolytes via orthogonal design of experiments and regression modeling. *ACS Materials Letters, 8*(2), 614–620. DOI: 10.1021/acsmaterialslett.5c01492
- Butenko, D., Zhang, X., Dove, M. T., Tseng, J.-C., Zhang, Y., Yu, P., Chen, J., Gu, C., Zhang, S., Lei, J., Ren, Y., Chen, Y., Zhu, J., & Xia, W. (2026). Investigating the structural evolution of lithium zirconium nitrochloride solid electrolytes for all-solid-state batteries. *Nature Communications, 17*, 5642. DOI: 10.1038/s41467-026-71879-x
- Curcio, A., Sabato, A. G., Eroles, M. N., Gonzalez-Rosillo, J. C., Morata, A., Tarancón, A., & Ciucci, F. (2022). Ultrafast crystallization and sintering of $Li_{1.5}Al_{0.5}Ge_{1.5}(PO_4)_3$ glass and its impact on ion conduction. *ACS Applied Energy Materials, 5*(11), 14466–14475. DOI: 10.1021/acsaem.2c03009
- de Klerk, N. J. J., van der Maas, E., & Wagemaker, M. (2018). Analysis of diffusion in solid-state electrolytes through molecular dynamics simulations, improvement of the Li-ion conductivity in β-Li_3PS_4 as an example. *ACS Applied Energy Materials, 1*(7), 3230–3242. DOI: 10.1021/acsaem.8b00457
- Dembitskiy, A. D., Humonen, I. S., Eremin, R. A., Aksyonov, D. A., Fedotov, S. S., & Budennyy, S. A. (2025). Benchmarking machine learning models for predicting lithium ion migration. *npj Computational Materials, 11*, 131. DOI: 10.1038/s41524-025-01571-z
- Deng, Z., Mishra, T. P., Mahayoni, E., Ma, Q., Tieu, A. J., Guillon, O., & de Souza, R. A. (2022). Fundamental investigations on the sodium-ion transport properties of mixed polyanion solid-state battery electrolytes. *Nature Communications, 13*, 4470. DOI: 10.1038/s41467-022-32190-7
- Ding, J., Gupta, M. K., Rosenbach, C., Lin, H.-M., Osti, N. C., Abernathy, D. L., Zeier, W. G., & Delaire, O. (2025). Liquid-like dynamics in a solid-state lithium electrolyte. *Nature Physics, 21*, 118–125. DOI: 10.1038/s41567-024-02707-6
- Dorai, A., Kim, S., Kuwata, N., Kawamura, J., Kisu, K., & Orimo, S.-I. (2024). Understanding ion

dynamics in closoborate-type lithium-ion conductors on different time-scales. *The Journal of Physical Chemistry Letters, 15*(18), 4864–4871. DOI: 10.1021/acs.jpclett.4c00754

- Dumett Torres, D., & Jain, P. K. (2018). Strain stabilization of superionicity in copper and lithium selenides. *The Journal of Physical Chemistry Letters, 9*(6), 1200–1205. DOI: 10.1021/acs.jpclett.8b00236
- Guan, C., Zong, J., Li, J., Ouyang, R., Zhao, Y., Huang, F., & Zhu, H. (2026). Triggering dynamically disordered lithium sublattice in superionic conductors. *Nature Communications, 17*, 4651. DOI: 10.1038/s41467-026-71304-3
- Gulino, V., Brighi, M., Dematteis, E. M., Murgia, F., Nervi, C., Černý, R., & Baricco, M. (2019). Phase stability and fast ion conductivity in the hexagonal $LiBH_4$–LiBr–LiCl solid solution. *Chemistry of Materials, 31*(14), 5133–5144. DOI: 10.1021/acs.chemmater.9b01035
- Han, F., Westover, A. S., Yue, J., Fan, X., Wang, F., Chi, M., Leonard, D. N., Dudney, N. J., Wang, H., & Wang, C. (2019). High electronic conductivity as the origin of lithium dendrite formation within solid electrolytes. *Nature Energy, 4*(3), 187–196. DOI: 10.1038/s41560-018-0312-z
- Hanghofer, I., Gadermaier, B., & Wilkening, H. M. R. (2019). Fast rotational dynamics in argyrodite-type Li_6PS_5X (X: Cl, Br, I) as seen by ^{31}P nuclear magnetic relaxation—On cation–anion coupled transport in thiophosphates. *Chemistry of Materials, 31*(12), 4591–4597. DOI: 10.1021/acs.chemmater.9b01435
- He, X., Zhu, Y., & Mo, Y. (2017). Origin of fast ion diffusion in super-ionic conductors. *Nature Communications, 8*, 15893. DOI: 10.1038/ncomms15893
- He, X., Zhu, Y., Epstein, A., & Mo, Y. (2018). Statistical variances of diffusional properties from ab initio molecular dynamics simulations. *npj Computational Materials, 4*, 18. DOI: 10.1038/s41524-018-0074-y
- Hogrefe, K., Gadermaier, B., Schneider, C., Bette, S., Lotsch, B. V., & Wilkening, H. M. R. (2025). A dynamically induced phase transition in $Na_4P_2S_6$—Ultrafast Na^+ mobility triggering rotor phase formation. *Journal of the American Chemical Society, 147*(32), 28799–28809. DOI: 10.1021/jacs.5c05339
- Huang, Y., Černý, R., Battaglia, C., & Remhof, A. (2023). Elucidating the pressure-induced enhancement of ionic conductivity in sodium closo-hydroborate electrolytes for all-solid-state batteries. *Journal of Materials Science, 58*(17), 7398–7406. DOI: 10.1007/s10853-022-08121-8
- Huo, C., Ma, L., Yao, Y., Cui, X., Liu, S., Deng, S., & Chen, J. (2024). Strain-enhanced low-temperature high ionic conductivity in perovskite nanopillar-array films. *Journal of the American Chemical Society, 146*(49), 33937–33944. DOI: 10.1021/jacs.4c12625
- Jacquet, Q., Cele, J., Casiez, L., Tardif, S., Medjahed, A., Pouget, S., Burghammer, M., Lyonnard, S., & Oukassi, S. (2025). Operando microimaging of crystal structure and orientation in all components of all-solid-state batteries. *Nature Communications, 16*, 11524. DOI: 10.1038/s41467-025-66306-6
- Kraft, M. A., Ohno, S., Zinkevich, T., Koerver, R., Culver, S. P., Fuchs, A., Senyshyn, A., Indris, S., Morgan, B. J., & Zeier, W. G. (2017). Influence of lattice polarizability on the ionic conductivity in the lithium superionic argyrodites Li_6PS_5X. *Journal of the American Chemical Society, 139*(31), 10909–10918. DOI: 10.1021/jacs.7b06327
- Kwak, H., Kim, J. S., Han, D., Kim, J. S., Park, J., Kwon, G., Bak, S. M., Heo, U., Park, C., Lee, H. W., Nam, K. W., Seo, D. H., & Jung, Y. S. (2023). Boosting the interfacial superionic conduction of halide solid electrolytes for all-solid-state batteries. *Nature Communications, 14*, 2459. DOI: 10.1038/s41467-023-38037-z
- Kwon, G., Gwon, H., Bae, Y., Jung, C., Ko, D.-S., Kim, M. G., Yoon, K., Yoon, G., Kim, S., Jung, I.-S., Lee, S., Kim, T., Kim, J.-S., Kim, T. Y., & Kim, Y. S. (2025). Disorder-driven sintering-free garnet-type solid electrolytes. *Nature Communications, 16*, 3256. DOI: 10.1038/s41467-025-58108-7
- Kwon, G., Gwon, H., Bae, Y., Jung, C., Ko, D.-S., Kim, M. G., Yoon, K., Yoon, G., Kim, S., Jung, I.-S., Lee, S., Kim, T., Kim, J.-S., Kim, T. Y., & Kim, Y. S. (2025). Disorder-driven sintering-free garnet-type solid electrolytes. *Nature Communications, 16*, 3256. DOI: 10.1038/s41467-025-58108-7
- Lacivita, V., Artrith, N., & Ceder, G. (2018). Structural and compositional factors that control the Li-ion conductivity in LiPON electrolytes. *Chemistry of Materials, 30*(20), 7077–7090. DOI: 10.1021/acs.chemmater.8b02812
- Lee, H. J., Darminto, B., Narayanan, S., Diaz-Lopez, M., Xiao, A. W., Chart, Y., Lee, J. H., Dawson, J. A., & Pasta, M. (2022). Li-ion conductivity in $Li_2OHCl_{1-x}Br_x$ solid electrolytes: Grains, grain boundaries and interfaces. *Journal of Materials Chemistry A, 10*, 11574–11586. DOI: 10.1039/D2TA01462A
- Lee, J., Ju, S., Hwang, S., You, J., Jung, J., Kang, Y., & Han, S. (2024). Disorder-dependent Li diffusion in Li_6PS_5Cl investigated by machine-learning potential. *ACS Applied Materials & Interfaces, 16*(35), 46442–46453. DOI: 10.1021/acsami.4c08865
- Lee, T., Qi, J., Gadre, C. A., Huyan, H., Ko, S.-T., Zuo, Y., Du, C., Li, J., Aoki, T., Wu, R., Luo, J., Ong, S. P., & Pan, X. (2023). Atomic-scale origin of the low grain-boundary resistance in perovskite solid electrolyte $Li_{0.375}Sr_{0.4375}Ta_{0.75}Zr_{0.25}O_3$. *Nature Communications, 14*, 1940. DOI: 10.1038/s41467-023-37115-6

- Lefevr, J., Cervini, L., Griffin, J. M., & Blanchard, D. (2018). Lithium conductivity and ion dynamics in $LiBH_4/SiO_2$ solid electrolytes studied by solid-state NMR and quasi-elastic neutron scattering and applied in lithium–sulfur batteries. *The Journal of Physical Chemistry C, 122*(27), 15264–15275. DOI: 10.1021/acs.jpcc.8b01507
- Li, F., Cheng, X., Lu, G., Yin, Y.-C., Wu, Y.-C., Pan, R., Luo, J.-D., Huang, F., Feng, L.-Z., Lu, L.-L., Ma, T., Zheng, L., Jiao, S., Cao, R., Liu, Z.-P., Zhou, H., Tao, X., Shang, C., & Yao, H.-B. (2023). Amorphous chloride solid electrolytes with high Li-ion conductivity for stable cycling of all-solid-state high-nickel cathodes. *Journal of the American Chemical Society, 145*(50), 27774–27787. DOI: 10.1021/jacs.3c10602
- Li, F., et al. (2023). Amorphous chloride solid electrolytes with high Li-ion conductivity for stable cycling of all-solid-state high-nickel cathodes. *Journal of the American Chemical Society, 145*, 27774–27787. DOI: 10.1021/jacs.3c10602
- Li, R., et al. (2025). A sodium superionic chloride electrolyte driven by paddle-wheel mechanism for solid-state batteries. *Nature Communications, 16*, 6633. DOI: 10.1038/s41467-025-61738-6
- Li, R., Xu, K., Wen, S., Tang, X., Lin, Z., Guo, X., Avdeev, M., Zhang, Z., & Hu, Y.-S. (2025). A sodium superionic chloride electrolyte driven by paddle-wheel mechanism for solid-state batteries. *Nature Communications, 16*, 6633. DOI: 10.1038/s41467-025-61738-6
- Liang, J., Li, X., Wang, S., Adair, K. R., Li, W., Zhao, Y., Wang, C., Hu, Y., Zhang, L., Zhao, S., Lu, S., Huang, H., Li, R., Mo, Y., & Sun, X. (2020). Site-occupation-tuned superionic Li_xScCl_{3+x} halide solid electrolytes for all-solid-state batteries. *Journal of the American Chemical Society, 142*(15), 7012–7022. DOI: 10.1021/jacs.0c00134
- Lin, X., et al. (2025). A family of dual-anion-based sodium superionic conductors for all-solid-state sodium-ion batteries. *Nature Materials, 24*, 83–91. DOI: 10.1038/s41563-024-02011-x
- Lin, X., Zhang, S., Yang, M., Xiao, B., Zhao, Y., Luo, J., Fu, J., Wang, C., Li, X., Li, W., Yang, F., Duan, H., Liang, J., Fu, B., Abdolvand, H., Guo, J., King, G., & Sun, X. (2025). A family of dual-anion-based sodium superionic conductors for all-solid-state sodium-ion batteries. *Nature Materials, 24*, 83–91. DOI: 10.1038/s41563-024-02011-x
- Liu, Z., Chien, P.-H., Wang, S., Song, S., Lu, M., Chen, S., Xia, S., Liu, J., Mo, Y., & Chen, H. (2024). Tuning collective anion motion enables superionic conductivity in solid-state halide electrolytes. *Nature Chemistry, 16*(10), 1584–1591. DOI: 10.1038/s41557-024-01634-6
- López, C., Rurali, R., & Cazorla, C. (2024). How concerted are ionic hops in inorganic solid-state electrolytes? *Journal of the American Chemical Society, 146*(12), 8269–8279. DOI: 10.1021/jacs.3c13279
- Ma, C., Yu, Z., Fang, J., Shi, Q., Wang, P., Liu, Y., Liu, Z., Monteiro, R., Parreira, L., Chen, H., Liu, Y., Lu, S., Feng, W., Zhu, H., & Zhao, Y. (2026). Coupled engineering of short-/long-range disorder in oxyhalides unlocks benchmark sodium superionic conductor. *Angewandte Chemie International Edition, 65*(2), e202518183. DOI: 10.1002/anie.202518183
- Mahmoud, M. M., Cui, Y., Rohde, M., Ziebert, C., Link, G., & Seifert, H. J. (2016). Microwave crystallization of lithium aluminum germanium phosphate solid-state electrolyte. *Materials, 9*(7), 506. DOI: 10.3390/ma9070506
- Malgope, S., Gupta, M. K., Mittal, R., Delaire, O., Shukla, R., Achary, S. N., Aouane, M., Tyagi, A. K., & Chaplot, S. L. (2026). Engineering ionic pathways by phonon–structure connection in perovskite solid electrolyte $Li_{0.29}La_{0.57}TiO_3$. *Communications Materials, 7*, 165. DOI: 10.1038/s43246-026-01164-3
- McGowan, J., Sampson, M., Salzwedel, D. M., Cogo, E., Foerster, V., & Lefebvre, C. (2016). PRESS peer review of electronic search strategies: 2015 guideline statement. *Journal of Clinical Epidemiology, 75*, 40–46. DOI: 10.1016/j.jclinepi.2016.01.021
- Morgan, B. J. (2021). Mechanistic origin of superionic lithium diffusion in anion-disordered Li_6PS_5X argyrodites. *Chemistry of Materials, 33*(6), 2004–2018. DOI: 10.1021/acs.chemmater.0c03738
- Muy, S., et al. (2018). Tuning mobility and stability of lithiumion conductors based on lattice dynamics. *Energy and Environmental Science, 11*, 850–859. DOI: 10.1039/C7EE03364H
- Novak, E., Daemen, L., Ramirez-Cuesta, A. J., Cheng, Y., Smith, R., Egami, T., & Jalarvo, N. (2022). Uncovering the hydride ion diffusion pathway in barium hydride via neutron spectroscopy. *Scientific Reports, 12*, 6194. DOI: 10.1038/s41598-022-10199-8
- Page, M. J., McKenzie, J. E., Bossuyt, P. M., Boutron, I., Hoffmann, T. C., Mulrow, C. D., Shamseer, L., Tetzlaff, J. M., Akl, E. A., Brennan, S. E., Chou, R., Glanville, J., Grimshaw, J. M., Hróbjartsson, A., Lalu, M. M., Li, T., Loder, E. W., Mayo-Wilson, E., McDonald, S., ... Moher, D. (2021). The PRISMA 2020 statement: An updated guideline for reporting systematic reviews. *BMJ, 372*, n71. DOI: 10.1136/bmj.n71
- Pham, K. H., Begum-Hudde, V., Lin, A. K., Spear, N. A., McClellan, J., Zuerch, M. W., Schleife, A., See, K. A., & Cushing, S. K. (2025). The dynamical role of optical phonons and sublattice screening in a solid-state ion conductor. *Journal of the American Chemical Society, 147*(30), 26456–26467. DOI: 10.1021/jacs.5c06064
- Puls, S., Nazmutdinova, E., Kalyk, F., Woolley, H. M., Thomsen, J. F., Cheng, Z., Fauchier-Magnan, A., Gautam, A., Gockeln, M., Ham, S.-Y., Hasan, M. T., Jeong, M.-G., Hiraoka, D., Kim, J. S., Kutsch,

T., Lelotte, B., Minnmann, P., Miß, V., Motohashi, K., ... Vargas-Barbosa, N. M. (2024). Benchmarking the reproducibility of all-solid-state battery cell performance. *Nature Energy, 9*, 1310–1320. DOI: 10.1038/s41560-024-01634-3

- Rethlefsen, M. L., Kirtley, S., Waffenschmidt, S., Ayala, A. P., Moher, D., Page, M. J., Koffel, J. B., & PRISMA-S Group. (2021). PRISMA-S: An extension to the PRISMA statement for reporting literature searches in systematic reviews. *Journal of the Medical Library Association, 109*(2), 174–200. DOI: 10.5195/jmla.2021.962
- Schweiger, L., Hogrefe, K., Gadermaier, B., Rupp, J. L. M., & Wilkening, H. M. R. (2022). Ionic conductivity of nanocrystalline and amorphous $Li_{10}GeP_2S_{12}$: The detrimental impact of local disorder on ion transport. *Journal of the American Chemical Society, 144*(22), 9597–9609. DOI: 10.1021/jacs.1c13477
- Schwietert, T. K., Gautam, A., Lavrinenko, A. K., Drost, D., Famprikis, T., Wagemaker, M., & Vasileiadis, A. (2024). Understanding the role of aliovalent cation substitution on the Li-ion diffusion mechanism in $Li_{6+x}P_{1-x}Si_xS_5Br$ argyrodites. *Materials Advances, 5*(5), 1952–1959. DOI: 10.1039/D3MA01042B
- Sebti, E., Evans, H. A., Chen, H., Richardson, P. M., White, K. M., Giovine, R., Koirala, K. P., Xu, Y., Gonzalez-Correa, E., Wang, C., Brown, C. M., Cheetham, A. K., Canepa, P., & Clément, R. J. (2022). Stacking faults assist lithium-ion conduction in a halide-based superionic conductor. *Journal of the American Chemical Society, 144*(13), 5795–5811. DOI: 10.1021/jacs.1c11335
- Song, S., Xue, W., Wang, Y., Wang, Z., Cui, Y., Long, Z., Shan, H., Hu, N., Wang, J., & Pan, F. (2025). All-climate all-solid-state batteries enabled by high-entropy amorphous oxyhalide solid electrolytes. *Green Chemistry, 27*. DOI: 10.1039/D5GC03551A
- Tanaka, Y., Ueno, K., Mizuno, K., Takeuchi, K., Asano, T., & Sakai, A. (2023). New oxyhalide solid electrolytes with high lithium ionic conductivity exceeding 10 mS cm^{-1} for all-solid-state batteries. *Angewandte Chemie International Edition, 62*, e202217581. DOI: 10.1002/anie.202217581
- Tang, W. S., Yoshida, K., Soloninin, A. V., Skoryunov, R. V., Babanova, O. A., Skripov, A. V., Dimitrievska, M., Stavila, V., Orimo, S.-I., & Udovic, T. J. (2016). Stabilizing superionic-conducting structures via mixed-anion solid solutions of monocarba-closo-borate salts. *ACS Energy Letters, 1*(4), 659–664. DOI: 10.1021/acsenergylett.6b00310
- Tani, K., Tada, T., & Takami, T. (2025). Fluoride superionic conduction in TlF with the new anti-α-CuBr structure containing intrinsic F vacancies. *Journal of Materials Chemistry A, 13*, 1478–1484. DOI: 10.1039/D4TA06334A
- Xu, Z., Chen, X., Zhu, H., and Li, X. (2022). Anharmonic cation–anion coupling dynamics assisted lithium-ion diffusion in sulfide solid electrolytes. *Advanced Materials, 34*, 2207411. DOI: 10.1002/adma.202207411
- Xu, Z., Duan, H., Dou, Z., Zheng, M., Lin, Y., Xia, Y., Zhao, H., & Xia, Y. (2023). Machine learning molecular dynamics simulation identifying weakly negative effect of polyanion rotation on Li-ion migration. *npj Computational Materials, 9*, 105. DOI: 10.1038/s41524-023-01049-w
- Zhang, B., Lin, Z., Dong, H., Wang, L.-W., & Pan, F. (2020). Revealing cooperative Li-ion migration in $Li_{1+x}Al_xTi_{2-x}(PO_4)_3$ solid-state electrolytes with high Al doping. *Journal of Materials Chemistry A, 8*, 342–348. DOI: 10.1039/C9TA09770H
- Zhang, S., et al. (2024). Amorphous oxyhalide matters for achieving lithium superionic conduction. *Journal of the American Chemical Society, 146*, 2977–2985. DOI: 10.1021/jacs.3c07343
- Zhang, S., Zhao, F., Chang, L.-Y., Chuang, Y.-C., Zhang, Z., Zhu, Y., Hao, X., Fu, J., Chen, J., Luo, J., Li, M., Gao, Y., Huang, Y., Sham, T.-K., Gu, M., Zhang, Y., King, G., & Sun, X. (2024). Amorphous oxyhalide matters for achieving lithium superionic conduction. *Journal of the American Chemical Society, 146*(5), 2977–2985. DOI: 10.1021/jacs.3c07343
- Zhang, W., Wu, X., Wang, C., Hu, S., Liu, Y., & Wang, L.-W. (2026). Constructing machine learning interatomic potentials with minimum amount of ab initio data. *npj Computational Materials, 12*, 174. DOI: 10.1038/s41524-026-02023-y
- Zhang, Z., Li, H., Kaup, K., Zhou, L., Roy, P.-N., & Nazar, L. F. (2020). Targeting superionic conductivity by turning on anion rotation at room temperature in fast ion conductors. *Matter, 2*(6), 1667–1684. DOI: 10.1016/j.matt.2020.04.027
- Zhao, F., et al. (2025). Anion sublattice design enables superionic conductivity in crystalline oxyhalides. *Science*. DOI: 10.1126/science.adt9678
- Zhu, C., Fuchs, T., Weber, S. A. L., Richter, F. H., Glasser, G., Weber, F., Butt, H.-J., Janek, J., & Berger, R. (2023). Understanding the evolution of lithium dendrites at $Li_{6.25}Al_{0.25}La_3Zr_2O_{12}$ grain boundaries via operando microscopy techniques. *Nature Communications, 14*, 1300. DOI: 10.1038/s41467-023-36792-7